

ResGS: Residual Densification of 3D Gaussian for Efficient Detail Recovery

Yanzhe Lyu Kai Cheng Xin Kang Xuejin Chen
University of Science and Technology of China



Figure 1. We propose ResGS, a pipeline to boost the rendering quality of 3D-GS [24] while improving efficiency. (a) The 3D-GS densification operations, split and clone, rely on binary selection and cannot adaptively address the challenges they encounter. (b) Our ResGS employs a single densification operation, residual split, that adaptively addresses under-reconstruction and over-reconstruction. (c) 3D-GS tends to generate Gaussians with sizes in small variation and low rendering quality. (d) From the same initialization, our method can **capture fine details** and **retrieve sufficient geometry** effectively while **reducing redundancy**.

Abstract

Recently, 3D Gaussian Splatting (3D-GS) has prevailed in novel view synthesis, achieving high fidelity and efficiency. However, it often struggles to capture rich details and complete geometry.

Our analysis reveals that the 3D-GS densification operation lacks adaptiveness and faces a dilemma between geometry coverage and detail recovery. To address this, we introduce a novel densification operation, **residual split**, which adds a downscaled Gaussian as a residual. Our approach is capable of adaptively retrieving details and complementing missing geometry. To further support this method, we propose a pipeline named ResGS. Specifically, we integrate a Gaussian image pyramid for progressive supervision and implement a selection scheme that prioritizes the densification of coarse Gaussians over time. Extensive experiments demonstrate that our method achieves SOTA rendering quality. Consistent performance improvements can be achieved by applying our residual split on various 3D-GS variants, underscoring its versatility and potential for

broader application in 3D-GS-based applications.

1. Introduction

Novel View Synthesis (NVS) has continued to be a hot topic throughout the years. Traditional methods like point clouds and meshes [4, 9, 14] can achieve high rendering speed but often lack fidelity. On the other hand, neural volumetric approaches [1, 31, 32] can achieve high fidelity for novel views but significantly sacrifice rendering efficiency. Recently, 3D-GS [24] has shown both high fidelity and fast rendering speed for novel view synthesis. However, 3D-GS still suffers from setbacks, often failing to capture fine details and recover complete geometry, as shown by red and orange rectangles in Fig. 1 and Fig. 2.

While various approaches [12, 13, 43, 48, 50] have been proposed to tackle these challenges and have significantly advanced the rendering quality of 3D-GS-based methods to SOTA levels, they have not modified the densification operation of 3D-GS. In this paper, we take a novel approach by revisiting and refining the densification operation to im-



Figure 2. **An illustration of the limitation of split and clone.** (a) selects between split and clone based on a high threshold, (b) a low threshold, and in (c) the densification operation is replaced as residual split. We provide visualizations of the final rendered image. A high threshold ensures sufficient structural coverage but causes over-reconstruction, leading to blurry rendering. Conversely, a low threshold mitigates blurry rendering but results in under-reconstruction, compromising coverage and creating a difficult trade-off. Our method, however, adaptively tackles both issues without facing this trade-off.

prove reconstruction quality.

The densification operation used in 3D-GS-based methods consists of two operations: split, designed to address over-reconstruction (where Gaussians cover too much area, resulting in a lack of detail), and clone, aimed at under-reconstruction (missing geometry). However, selecting between the two operations is challenging. 3D-GS-based methods rely on a threshold-based decision mechanism. As illustrated in Fig. 1 (a), Gaussians whose scale $s = \max(s_x, s_y, s_z)$ is larger than a predefined threshold τ_s undergo split, while those below it use clone. Due to its simplicity, the selected operation might be suboptimal and bring a dilemma in threshold selection. As highlighted by the red rectangles in Fig. 2 (a), a high threshold results in insufficient split, which prevents the model from capturing fine details, leading to blurry artifacts. On the other hand, a low threshold reduces clone operations, leading to missing geometry, as illustrated in the orange boxes in Fig. 2 (b). This dilemma limits the rendering quality. Furthermore, 3D-GS tends to first split and then clone, resulting in objects being fitted with Gaussians of similar scales. As highlighted by the blue rectangles in Fig. 1, 3D-GS fits textureless areas with an excessive number of small Gaussians, which is redundant.

To tackle the aforementioned problems, we propose residual split, a novel densification operation. As illustrated in Fig. 1 (b), the core idea is that for any under-optimized Gaussian, we spawn a downscaled replica as a residual component while reducing the original Gaussian’s opacity. This simultaneously expands spatial coverage and injects finer details, eliminating the split/clone dilemma.

However, directly applying residual split does not pro-

duce significant improvements. This is due to the inefficiency of initialization in 3D-GS. At early iterations, the scene is represented by a few coarse Gaussians that face both over-reconstruction and under-reconstruction. Gaussians added through densification are challenging to optimize, as they must address both issues simultaneously. It’s desired to develop an approach that decouples coverage and detail optimization.

Correspondingly, we propose a coarse-to-fine training pipeline, **ResGS**, that progressively shifts the focus of training, facilitating optimization. Firstly, we structure the training process into stages, employing multi-scale images for gradual supervision, ensuring that the early stages focus on the overall structure and the later stages focus on details. Secondly, we develop a progressive Gaussian selection scheme for densification, which gradually encourages coarser Gaussians to undergo further refinement. Therefore, finer structures are introduced at later iterations, avoiding premature optimization. These two techniques simplify optimization and thereby improve rendering quality.

Our contributions are summarized as follows:

- We propose a novel densification operation for 3D Gaussians based on a residual strategy to overcome the limitations of fixed threshold for determining split or clone in 3D-GS;
- We develop a coarse-to-fine training pipeline, ResGS, equipped with residual split, which incorporates an image-pyramid-based supervision schedule and a Gaussian selection scheme to enhance rendering quality;
- Our method achieves SOTA rendering quality in NVS on three datasets, including Mip-NeRF360 [1], Tanks&Temples [25], and DeepBlending [18]. Further-

more, applying residual split to multiple 3D-GS variants consistently brings performance improvements, demonstrating that our new densification operation is more effective than densification with a fixed scale threshold.

2. Related Work

2.1. Novel View Synthesis

Novel view synthesis (NVS) aims to acquire novel view images for a scene through a set of multi-view images. As a pioneer, NeRF [31] introduced an MLP-based implicit representation. More specifically, it uses an MLP to predict the color and opacity of a point in a scene and uses differentiable volume rendering to render images. Due to its photo-realistic quality, it has been extensively studied [1, 2, 6–8, 22, 27, 47]. However, NeRF-based methods often suffer from long training and rendering time. Therefore, many works [19, 20, 33, 34] have been proposed to extend NeRF into real-time rendering.

Recently, 3D-GS [24] has stirred an evolution in the field by achieving both high-fidelity and real-time rendering. Due to its high performance, many works have enabled 3D-GS into many downstream tasks such as SLAM [30, 41], 3D generation [10, 37, 44, 52], 4D scene modeling [16, 26, 39, 42], and surface reconstruction [15, 21].

However, the original 3D-GS still has limitations, and myriad works have been proposed to increase the render quality and efficiency of 3D-GS. Mip-Splatting [46] introduced a 2D dilation filter and a 3D smoothing filter to mitigate aliasing and artifacts caused by changes in focal length. Scaffold-GS [29] proposed the concept of neural Gaussians which is to tie Gaussians around an anchor and use an MLP to predict its attributes. Thus, the model is more robust to significant view changes and can improve rendering quality. AbsGS [43] discovered that when accumulating the view space gradients used in densification through pixels, there could be a collision, for gradients at various pixels might have different positivities. They applied an absolute function before summing through pixels to mitigate the issue. Pixel-GS [50] analyzed 3D-GS artifacts from the pixel perspective and introduced a method to select Gaussians for densification based on this analysis. GaussianPro [11] introduced a progressive propagation strategy to propagate Gaussians to under-initialized areas. To reduce redundancy and increase rendering quality, Mini-Splatting [13] proposed a densification and simplification algorithm to reorganize Gaussians’ spatial positions.

With the emergence of numerous works focused on optimizing NeRF and 3D-GS, progressive training schedules—proven effective in multiple scenarios [3, 17, 23, 36] have earned attention.

2.2. Progressive Training in NVS

Several progressive training schedules have been explored upon NeRF-based methods. BungeeNeRF [40] captured different levels of details in large city-scale datasets by gradually adding closer views to the training views and appending residual blocks to the MLP throughout the training process. Pyramid NeRF [51] proposed a progressive subdivision of the scene while utilizing an image pyramid to gradually add high-frequency information to the scene. BARF [28] proposed a scheduling approach to progressively incorporate higher frequency components in positional encoding, enabling the training of NeRFs without requiring camera poses.

Recently, with the prevalence of 3D-GS, many progressive training pipelines have been proposed. Octree-GS [35] proposed an Octree-based 3D-GS approach, and the Octree depth is progressively deepened. FreGS [48] designed a progressive frequency regulation for 3D-GS which is to calculate the loss of rendered images in the frequency domain and gradually add higher frequency components.

3. Our Method

3.1. Preliminaries

3D Gaussian Splatting. The 3D-GS work[24] represents a 3D scene with a set of anisotropic 3D Gaussians for fast and high-quality rendering. Each Gaussian primitive consists of two parameters, mean μ and covariance matrix Σ , representing its position and shape:

$$G(\mathbf{x}) = e^{-\frac{1}{2}(\mathbf{x}-\mu)^T \Sigma^{-1}(\mathbf{x}-\mu)}. \quad (1)$$

To model the positive semi-definite property of the covariance matrix Σ , a scaling matrix \mathbf{S} and a rotation matrix \mathbf{R} is used as:

$$\Sigma = \mathbf{R} \mathbf{S} \mathbf{S}^T \mathbf{R}^T, \quad (2)$$

where a 3D vector \mathbf{s} is used for the scaling matrix \mathbf{S} .

Furthermore, each Gaussian also contains a spherical harmonics coefficients SH and opacity o . In rendering, tile-based rasterization is applied: 3D Gaussians $G(\mathbf{x})$ are projected as 2D Gaussians $G'(\mathbf{x})$ on the image plane. A view-dependent color c is then derived from SH , and the 2D Gaussians are sorted by depth and rendered using alpha-blending:

$$C(\mathbf{x}) = \sum_{i \in N_{\mathbf{x}}} c_i \alpha_i(\mathbf{x}) \prod_{j=1}^{i-1} (1 - \alpha_j(\mathbf{x})), \quad (3)$$

$$\alpha_i(\mathbf{x}) = c_i G'_i(\mathbf{x})$$

where \mathbf{x} is a pixel position in the rendered image, $C(\mathbf{x})$ the color of the pixel, and $N_{\mathbf{x}}$ the number of Gaussians that covers \mathbf{x} .

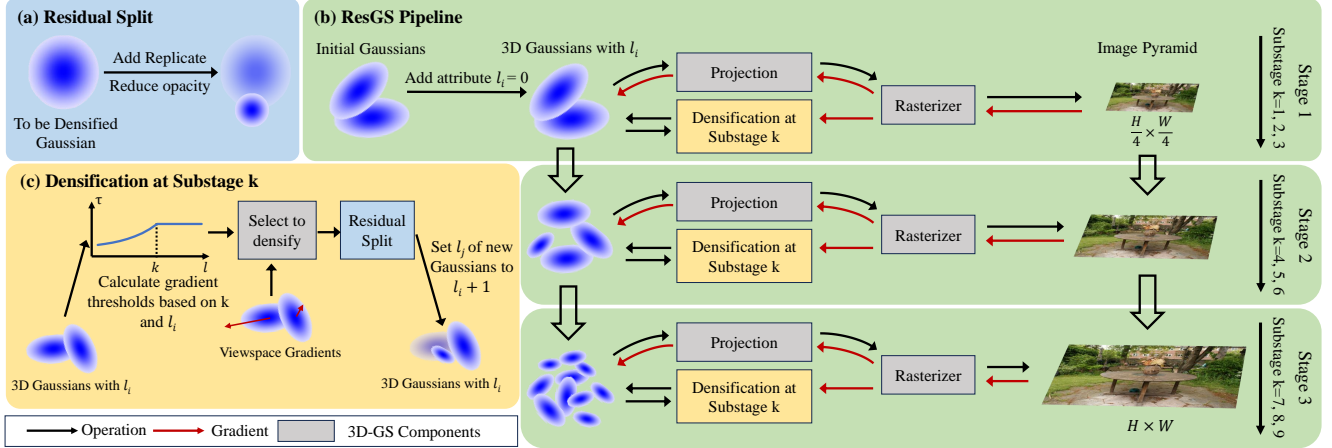


Figure 3. **Overview of our ResGS pipeline.** (a) The core of our pipeline, residual split, involves adding a downscaled replicate and then reducing the opacity of the original Gaussian. (b) We assign initial Gaussians a temporary attribute $l_i = 0$ for densification selection, which is discarded after training. Next, the pipeline is split into L ($L = 3$) stages, with each stage trained on images downscaled using an image pyramid. Furthermore, we divide a single stage evenly into K ($K = 3$) substages for use in selecting Gaussians to densify. (c) The points selected for densification are determined by the substage k , l_i and viewspace gradients of Gaussians. residual split is performed upon selected Gaussians, and l_j would be assigned to new Gaussians.

During the training process, 3D Gaussians are periodically densified. 3D-GS calculates the average viewspace gradients ΔL_i over a certain number (e.g. 100) of iterations to determine whether to perform densification. If ΔL_i exceeds threshold τ , a split or clone action is triggered. The split operation addresses over-reconstruction, where excessive space is covered, while clone addresses under-reconstruction, where additional spatial coverage is needed. To determine whether to split or clone, 3DGS[24] sets a threshold $\tau_s = kR$, where k is a predefined factor and R is the scene extent. Split occurs when the scale $s = \max(s_x, s_y, s_z)$ of a Gaussian surpasses a threshold τ_s . Clone is applied when $s < \tau_s$.

3.2. ResGS

We propose ResGS, a coarse-to-fine pipeline to boost the rendering quality of 3D-GS with a novel residual densification operation. Fig. 3 shows the overview of our method. We propose a novel densification operation, residual split, (Sec. 3.2.1), to tackle the limitations of the 3D-GS densification operation. Furthermore, we introduce a split-stage supervision schedule to add information to the scene gradually (Sec. 3.2.2). We also design a Gaussian selection scheme that progressively encourages densification for coarse Gaussians to enhance details, as described in Sec. 3.2.3.

3.2.1. Residual Split

The core idea of our densification operation is to generate downscaled Gaussians as residuals to supplement those requiring densification. The newly added Gaussian adap-

tively enhances the reconstructed model, allowing the scene to be refined as needed. The method is named as residual split. As illustrated in Fig. 3 (a), for a to-be-densified Gaussian G_i , our densification operation consists of two steps. Firstly, we add a down-scaled replicate G_j . Specifically, its opacity o_j , rotation \mathbf{R}_j , spherical harmonics coefficients SH_j would be same as G_i , μ_j is sampled using the original 3D Gaussian as a PDF for sampling, and \mathbf{S}_j is defined as \mathbf{S}_i divided by a set factor λ_s :

$$\begin{aligned} \mathbf{S}_j &= \frac{1}{\lambda_s} \mathbf{S}_i \\ \mathbf{R}_j &= \mathbf{R}_i, SH_j = SH_i, o_j = o_i \\ \mu_j &\sim \mathcal{N}(\mu_i, \Sigma_i) \end{aligned} \quad (4)$$

where Σ_i is the covariance matrix of G_i . Then, to tackle the density increase in the overlap of the two Gaussians, we reduce the opacity of the original Gaussian. This is accomplished by multiplying its opacity by a specified factor β :

$$o'_i = \beta o_i \quad (5)$$

Unlike clone and split which lack adaptiveness, residual split can fill in missing geometry and recover details adaptively without requiring a trade-off, as shown in Fig. 2 (c). We further illustrate this using intermediate results, as shown in Fig. 4. In areas where details are challenging to recover, down-scaled Gaussians of finer granularity are progressively introduced to refine and reveal intricate details. On the other hand, since densification does not change the scale of the original Gaussian, the total coverage is increased after densification, helping to reconstruct missing

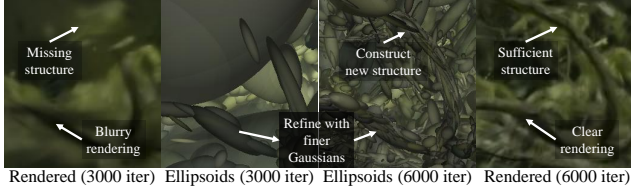


Figure 4. **Intermediate results after applying residual split.** We saved the Gaussians at 3,000 and 6,000 iterations after applying residual split. As observed, residual split can adaptively handle over-reconstruction and under-reconstruction by refining blurry regions with finer Gaussians while also effectively reconstructing missing structures. **Zoom in for better view.**

structures. Moreover, our method’s nonidentical approach with hierarchical Gaussians of varying scales enables efficient shape fitting. As illustrated by the blue rectangles in Fig. 1, this hierarchy allows us to fill textureless regions with a few large Gaussians, significantly reducing redundancy. Consequently, our approach delivers higher rendering quality while using fewer Gaussians.

3.2.2. Image Pyramid as Supervision

Building on our motivation in Sec. 1, we designed a coarse-to-fine supervision schedule that gradually integrates information into the scene. Specifically, based on the original multi-view training pictures, we build an image pyramid $\{IP_i\}_{i=1}^L$ consisting of L layers. IP_i corresponds to the set of images at different viewpoints in layer i . IP_L is the set of original pictures:

$$IP_i = \{P_i^v\}_{v \in V} \quad (6)$$

where V is the set of viewpoints and P_i^v refers to the picture at viewpoint v in the i th layer. Let (H_L^v, W_L^v) be the resolution of P_L^v , and (H_i^v, W_i^v) represent the resolution of P_i^v . Then there is:

$$(H_i^v, W_i^v) = (H_L^v/2^{L-i}, W_L^v/2^{L-i}) \quad (7)$$

Correspondingly, our training process is divided into L stages. At stage i , we train our model under the supervision of IP_i , increasing the resolution of the training pictures throughout the stages. Due to the variation of frequency bandwidth in different levels in the image pyramid, high-frequency information is gradually added to the scene. Thus, we can force our model to learn coarse and low-frequency features at early stages and construct an overall structure of the whole scene. At later stages, the focus shifts to capturing high-frequency components, carving details above the coarse expression.

3.2.3. Varying Gradient Threshold

To further emphasize progressive training, an incremental approach for selecting Gaussians to densify is designed.

Specifically, as iterations progress, the model’s focus gradually shifts toward finer details. To support this, we aim to encourage the densification of coarse Gaussians to capture more detail over time. Due to the nonidentical of our residual split, we can expect the generated Gaussians to be finer than the original ones. This allows us to track the relative fineness level of Gaussians, denoted as l_i . We assign l_i of initial Gaussians to 0. If the level of the Gaussian being densified is l_i , we assign the newly added Gaussian a level of $l_i + 1$. Thus, as l_i gets higher, Gaussians tend to be smaller and finer. Note that l_i is only utilized during training and discarded afterward.

A single stage is then divided evenly into K substages, creating $L \times K$ substages in total. The gradually increasing substage can be seen as an indicator of the scene details level. At substage k , we promote additional densification for Gaussians with $l_i < k$ and prioritize those at lower levels, achieved by applying varying gradient thresholds. Specifically, the threshold $\tau_{k,i}$ for a Gaussian G_i is set as:

$$\tau_{k,i} = \begin{cases} \tau, & l_i \geq k \\ \frac{\tau}{\alpha^{k-l_i}}, & l_i < k \end{cases} \quad (8)$$

where τ is a set threshold and $\alpha > 1$ is a chosen value.

4. Experiments

4.1. Experiment Settings

Following previous works [13, 24, 29, 35, 43, 48], evaluation of our model was done on three datasets, including all nine scenes from Mip-NeRF360 [1], two scenes from Tanks&Temples [25], and two scenes from DeepBlending [18]. The test and train splits follow those of the original 3D-GS [24], and the image resolution is also maintained as in 3D-GS.

Three commonly used metrics were used to quantify the fidelity of rendered images: PSNR, SSIM [38], and LPIPS [49]. We also report the memory consumption as an indicator of the number of Gaussians.

We trained three versions of our model: two with AbsGS [43], leveraging its enhanced indication of Gaussians for densification—one standard version and one small version with higher gradient thresholds—and a third version using 3D-GS as the baseline. We applied the periodic opacity reduction from AbsGS across all three versions, as it proved to be a more effective alternative to the opacity reset used in 3D-GS. Additionally, we extended this reduction beyond the densification phase, finding it further minimized redundancy without compromising fidelity. Following all 3D-GS-like methods, we trained our model for 30k iterations. The densification stops at 12000 iterations. For the version with AbsGS, τ was set to 0.00067, the small version

Table 1. **Quantitative comparison to previous methods on real-world datasets.** Our method achieves SOTA in the Mip-NeRF360 dataset and comparable results with SOTA on the Tanks&Temples and Deep Blending datasets. * indicates results generated by retrained models for different rendering resolution.

Dataset Method Metrics	Mip-NeRF360				Tanks&Temples				Deep Blending			
	PSNR \uparrow	SSIM \uparrow	LPIPS \downarrow	Mem.	PSNR \uparrow	SSIM \uparrow	LPIPS \downarrow	Mem.	PSNR \uparrow	SSIM \uparrow	LPIPS \downarrow	Mem.
Plenoxels	23.08	0.626	0.463	2.1GB	21.08	0.719	0.379	2.3GB	23.06	0.795	0.510	2.7GB
Instant-NGP	25.59	0.699	0.331	48MB	21.92	0.745	0.305	48MB	24.96	0.817	0.390	48MB
Mip-NeRF360	27.69	0.792	0.237	8.6MB	22.22	0.759	0.257	8.6MB	29.40	0.901	0.245	8.6MB
Scaffold-GS*	27.69	0.812	0.225	176MB	23.96	0.853	0.177	87MB	30.21	0.906	0.254	66MB
Octree-GS*	27.52	0.812	0.218	124MB	24.52	0.866	0.153	84MB	30.41	0.913	0.238	93MB
3D-GS	27.21	0.815	0.214	734MB	23.14	0.841	0.183	411MB	29.41	0.903	0.243	676MB
AbsGS	27.49	0.820	0.191	728MB	23.73	0.853	0.162	304MB	29.67	0.902	0.236	444MB
Pixel-GS*	27.52	0.822	0.191	1.32GB	23.78	0.853	0.151	1.06GB	28.91	0.892	0.250	1.09GB
FreGS	27.85	0.826	0.209	-	23.96	0.849	0.178	-	29.93	0.904	0.240	-
Mini-Splatting-D	27.51	0.831	0.176	1.11GB	23.23	0.853	0.140	1.01GB	29.88	0.906	0.211	1.09GB
Ours-Small (AbsGS)	27.94	0.830	0.191	342MB	24.33	0.862	0.150	187MB	30.01	0.906	0.234	289MB
Ours (3D-GS)	28.00	0.831	0.187	600MB	24.26	0.865	0.141	354MB	29.93	0.903	0.232	596MB
Ours (AbsGS)	28.00	0.833	0.174	698MB	24.38	0.867	0.132	351MB	29.91	0.902	0.227	586MB

to 0.0016; for the version with 3D-GS, τ was set to 0.00028. L was set to 3 and K was set to 3. Our first stage lasts for 2500 iterations, the second stage for 3500 iterations, and the rest iterations are in the last stage. A 500-iteration warm-up phase was introduced between stages with densification disabled. α was set to $2^{\frac{1}{3}}$, λ_s was set to 1.6 and β was set to 0.3. The loss function remains the same as in 3D-GS [24], consisting of a combination of \mathcal{L}_1 and D-SSIM losses. All experiments were done on an NVIDIA RTX3090 GPU.

4.2. Comparisons

To assess the effectiveness of our method, we compared it with several 3D-GS variants: 3D-GS [24], Scaffold-GS [29], Octree-GS [35], FreGS [48], AbsGS [43], Pixel-GS [50] and Mini-Splatting-D [13]. Note that Scaffold-GS and Octree-GS use a latent representation rather than the original 3D-GS representation. Some radiance-field-based methods are also selected for comparison, including Plenoxels [45], Instant-NGP [32] and Mip-NeRF360 [1]. We found that the resolution of Mip-NeRF360 dataset images varies across different works. Following the resolution setup in the 3D-GS work, we retrain some models on the Mip-NeRF360 dataset. Additionally, for works that did not report their storage, we obtained and reported it based on their released code.

Quality Comparisons. In Table 1, we present quantitative results comparing the rendering quality of our method with other approaches. From the table, we can see that our method achieves SOTA performance across all metrics on the Mip-NeRF360 [1] dataset. On the Tanks&Temples [25] dataset, we also achieve the best SSIM and LPIPS metrics, which closely reflect human perception. In the Deep Blending [18] dataset, while our method does not achieve the highest score, it shows a notable improvement over

Table 2. **Efficiency comparison with former methods.**

Dataset Method Metrics	Mip-NeRF360		Tanks&Temples		Deep Blending	
	FPS	Time	FPS	Time	FPS	Time
Octree-GS*	119	29m55s	126	23m8s	151	34m38s
Scaffold-GS*	103	23m53s	137	15m37s	141	19m40s
3D-GS	103	27m16s	127	15m34s	101	24m48s
AbsGS	132	28m48s	193	13m35s	185	22m3s
Mini-Splatting-D	74	34m42s	75	27m39s	100	30m37s
Pixel-GS*	65	40m6s	70	29m29s	70	34m1s
Ours-Small (AbsGS)	141	20m56s	206	11m35s	202	19m26s
Ours (AbsGS)	100	29m24s	150	16m29s	153	23m33s

the baseline. Additionally, our model variant without AbsGS [43] maintains similar performance to the full model, with only a slight reduction in LPIPS. Notably, our smaller model version achieves strong performance with reduced memory usage, showcasing the efficiency and scalability of our approach. In Fig. 5, we present qualitative comparisons between our method and several 3D-GS variants [24, 43, 50] across various scenes, including both indoor and outdoor settings. It is evident that our model captures finer details, as shown in the second, third, and fourth rows, constructs missing geometry more effectively (last row), and achieves more accurate geometry reconstruction (first row).

Efficiency Comparisons. Here, we provide the computational costs of our method in comparison with other approaches. The results are shown in Table 2. From the table, we can see that our method involves a slight increase in training time while delivering much higher rendering quality than methods with lower rendering quality like 3D-GS [24] and AbsGS [43]. Our method is also significantly more efficient than other methods like Mini-Splatting-D [13], with comparable rendering quality. Notably, our small model provides the fastest FPS and shortest training time in

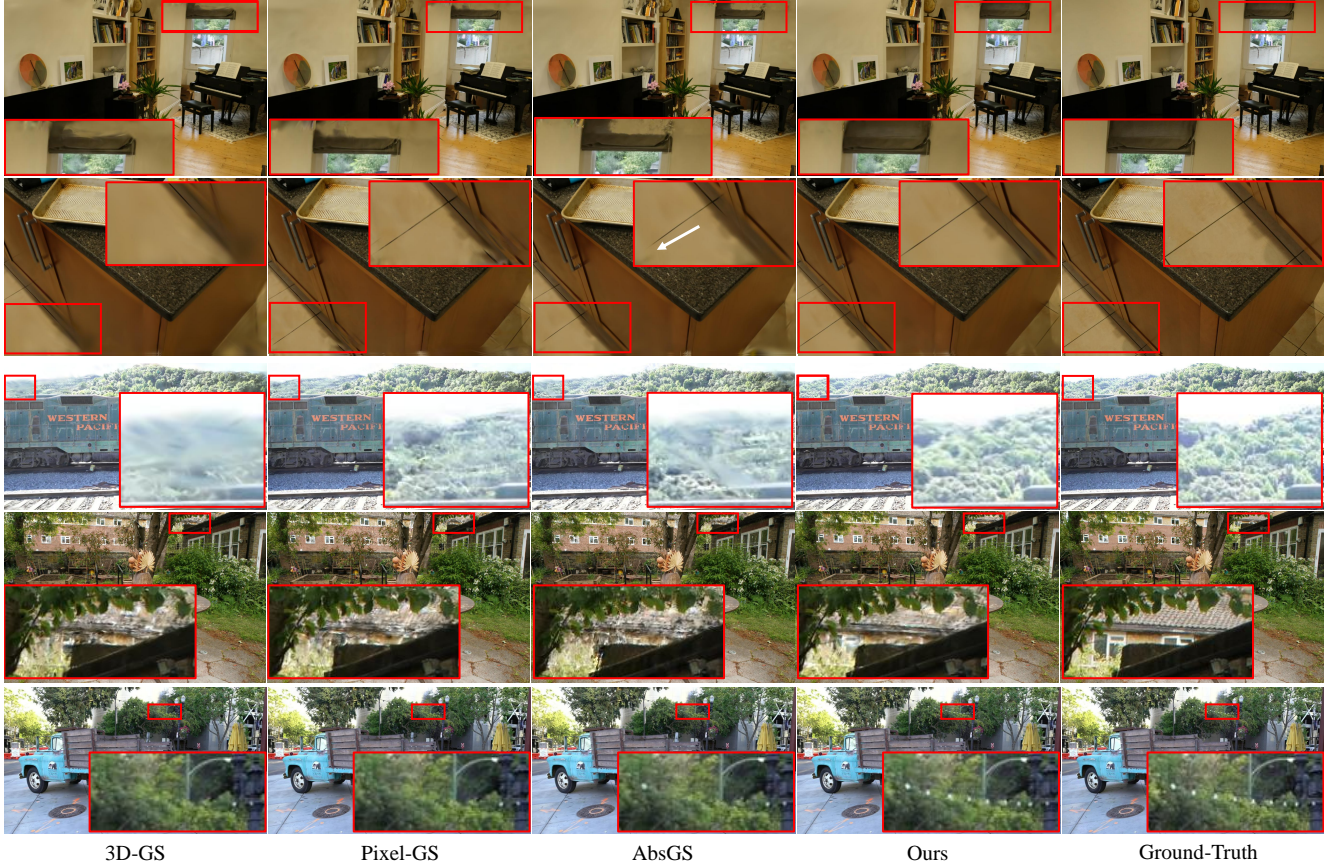


Figure 5. **Qualitative comparisons of ResGS with three 3D-GS variations on a variety of indoor and outdoor scenes.** Our approach captures more intrinsic details and acquires more complete geometry in complex scenes.

Table 3. **Analyzing residual split upon multiple 3D-GS variants.** The performance consistently increases on these pipelines, indicating that our Residual split is a better densification operation. **3D-GS[†]** indicates a retrained version of 3D-GS [24] for better performance.

Dataset Method Metrics	Mip-NeRF360				Tanks&Temples				Deep Blending			
	PSNR \uparrow	SSIM \uparrow	LPIPS \downarrow	Mem	PSNR \uparrow	SSIM \uparrow	LPIPS \downarrow	Mem	PSNR \uparrow	SSIM \uparrow	LPIPS \downarrow	Mem
3D-GS	27.21	0.815	0.214	734MB	23.14	0.841	0.183	411MB	29.41	0.903	0.243	676MB
3D-GS[†]	27.38	0.813	0.215	821MB	23.66	0.844	0.179	434MB	29.48	0.900	0.247	663MB
3D-GS + residual split	27.44	0.813	0.216	586MB	23.76	0.845	0.178	318MB	29.75	0.902	0.240	546MB
AbsGS	27.49	0.820	0.191	728MB	23.73	0.853	0.162	304MB	29.67	0.902	0.236	444MB
AbsGS + residual split	27.71	0.827	0.185	712MB	24.05	0.857	0.161	285MB	29.68	0.905	0.234	421MB
Pixel-GS*	27.52	0.822	0.191	1.32GB	23.78	0.853	0.151	1.06GB	28.91	0.892	0.250	1.09GB
Pixel-GS + residual split	27.62	0.821	0.191	1.00GB	24.05	0.856	0.148	754MB	29.75	0.899	0.235	914MB
Mini-Splatting-D	27.51	0.831	0.176	1.11GB	23.23	0.853	0.140	1.01GB	29.88	0.906	0.211	1.09GB
Mini-Splatting-D + residual split	27.64	0.831	0.176	1.04GB	23.49	0.853	0.140	967MB	29.94	0.903	0.210	1.02GB

all compared methods while maintaining high fidelity.

4.3. Analysis

4.3.1. Residual Split

Compatibility. We analyze the compatibility of our novel densification operation by replacing split and clone in multiple 3D-GS variants [13, 24, 43, 50] with residual split. The hyperparameters were kept the same as in the original pipelines. The results are shown in Table 3. The table shows

that our method leads to a notable increase in PSNR metrics across all pipelines, while for other metrics, some exhibit improvements, and others remain approximately the same. Additionally, memory consumption is reduced after incorporating residual split compared to the original pipeline. This underscores our method’s ability to improve rendering quality and reduce redundancy, while also demonstrating its compatibility and potential for broader application across 3D-GS-oriented works as an effective alternative to

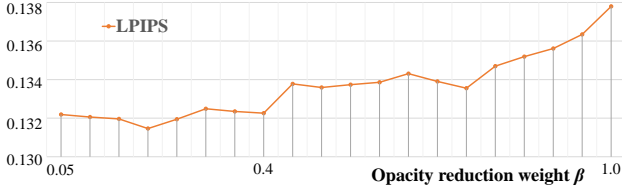


Figure 6. **Impact of the opacity reduction weight β for residual split.**



Figure 7. **Impact of the scale reduction factor λ_s for residual split.**

Table 4. **Ablation Study on our pipeline.** Here, **IP** denotes image pyramid supervision, **RS** represents using residual split for densification, and **VT** indicates applying varying gradient threshold. Each component contributes to our method’s effectiveness.

Dataset Method Metrics	Mip-NeRF360		
	PSNR \uparrow	SSIM \uparrow	LPIPS \downarrow
Base	27.41	0.817	0.189
Base + RS	27.66	0.825	0.183
Base + IP	27.54	0.823	0.182
Base + RS + IP	27.88	0.831	0.178
Base + RS + IP + VT (full)	28.00	0.833	0.174

split and clone.

Hyperparameter Sensitivities. Since residual split involves some hyperparameters: opacity reduction weight β and scale reduction factor λ_s , we conducted a corresponding sensitivity analysis. We tested our method upon the Tanks&Temples dataset while applying different $\beta \in [0.05, 1.0)$ and $\lambda_s \in [1.05, 2.0]$. All the models are trained with similar storage. The LPIPS scores are shown in Fig. 6 and 7. As shown in the figures, LPIPS scores remain relatively stable when $\beta < 0.4$ and $\lambda_s > 1.55$. These results indicate that our method is robust to hyperparameter variations, with only a 0.006 difference in LPIPS between the best and worst cases, and a relatively broad range where rendering quality remains optimal.

4.3.2. Ablation Studies

To assess the effectiveness of individual modules in our proposed pipeline—residual split, image pyramid as supervision, and varying gradient threshold—ablation studies on the Mip-NeRF360 [1] dataset were conducted. For the vary-

ing gradient threshold, we only conducted studies on its removal, as it is highly interdependent with the other two modules. The results are shown in Table 4. It is evident that both residual split and the image pyramid supervision individually enhance the quality of our baseline. However, we observe that adding image pyramid supervision alone does not lead to significant improvements. This is because the split-and-clone operations do not perform well within a coarse-to-fine schedule. In the early stages, when the overall structure is still being constructed, split is primarily chosen, which exacerbates the issue rather than improving it. On the other hand, in later iterations, when fine details need to be recovered, clone is selected and does not address the issue properly. Conversely, residual split works perfectly due to its adaptiveness. This is evident from the notable improvement of **Base + RS + IP** over both **Base + IP** and **Base + RS**, which also shows that a coarse-to-fine schedule supplements residual split as expected. Additionally, applying the varying gradient threshold further boosts performance. In conclusion, each module contributes to improved results.

4.4. Discussions and Limitations

Our results show that our method significantly improves rendering quality on the Mip-NeRF360 [1] and Tanks&Temples [25] datasets. However, for Deep Blending [18], our method did not yield a significant boost in performance. This variation is primarily due to the challenges specific to each dataset: Mip-NeRF360 and Tanks&Temples require capturing fine textures and recovering missing geometry, whereas Deep Blending focuses on handling occlusions and reconstructing accurate geometry in weakly textured areas. Our method mainly contributes to retrieving fine details and sufficient geometry and does not address the issue of occlusion and weak-textured areas, suggesting it to be a topic for future optimization.

5. Conclusion

In this paper, we analyzed the limitations of the current 3D-GS densification operation. To address these issues, we propose residual split, a residual empowered densification operation that adaptively handles both over-reconstruction and under-reconstruction. Additionally, we introduce ResGS, a coarse-to-fine 3D-GS pipeline to supplement residual split. Specifically, we use an image pyramid for supervision to gradually recover the overall structure to fine details during Gaussian optimization. We also design a Gaussian selection scheme to further densify coarse Gaussians progressively. Experiments show our pipeline achieves SOTA rendering quality while residual split is highly compatible with other 3D-GS variants.

References

- [1] Jonathan T. Barron, Ben Mildenhall, Matthew Tancik, Peter Hedman, Ricardo Martin-Brualla, and Pratul P. Srinivasan. Mip-nerf: A multiscale representation for anti-aliasing neural radiance fields. *2021 IEEE/CVF International Conference on Computer Vision (ICCV)*, pages 5835–5844, 2021. [1](#), [2](#), [3](#), [5](#), [6](#), [8](#)
- [2] Jonathan T. Barron, Ben Mildenhall, Dor Verbin, Pratul P. Srinivasan, and Peter Hedman. Zip-nerf: Anti-aliased grid-based neural radiance fields. *2023 IEEE/CVF International Conference on Computer Vision (ICCV)*, pages 19640–19648, 2023. [3](#)
- [3] Yoshua Bengio, Jérôme Louradour, Ronan Collobert, and Jason Weston. Curriculum learning. In *International Conference on Machine Learning*, 2009. [3](#)
- [4] Mario Botsch, Alexander Sorkine-Hornung, Matthias Zwicker, and Leif Kobbelt. Eurographics symposium on point-based graphics (2005) high-quality surface splatting on today’s gpus. [1](#)
- [5] Samuel Rota Bulò, Lorenzo Porzi, and Peter Kotschieder. Revising densification in gaussian splatting. *ArXiv*, abs/2404.06109, 2024. [1](#)
- [6] Eric R. Chan, Connor Z. Lin, Matthew A. Chan, Koki Nagano, Boxiao Pan, Shalini De Mello, Orazio Gallo, Leonidas Guibas, Jonathan Tremblay, Sameh Khamis, Tero Karras, and Gordon Wetzstein. Efficient geometry-aware 3D generative adversarial networks. In *CVPR*, 2022. [3](#)
- [7] Anpei Chen, Zexiang Xu, Fuqiang Zhao, Xiaoshuai Zhang, Fanbo Xiang, Jingyi Yu, and Hao Su. Mvsnerf: Fast generalizable radiance field reconstruction from multi-view stereo. *2021 IEEE/CVF International Conference on Computer Vision (ICCV)*, pages 14104–14113, 2021.
- [8] Shuhong Chen, Kevin Zhang, Yichun Shi, Heng Wang, Yiheng Zhu, Guoxian Song, Sizhe An, Janus Kristjansson, X. Yang, and Matthias Zwicker. Panic-3d: Stylized single-view 3d reconstruction from portraits of anime characters. *2023 IEEE/CVF Conference on Computer Vision and Pattern Recognition (CVPR)*, pages 21068–21077, 2023. [3](#)
- [9] Shenchang Eric Chen and Lance R. Williams. View interpolation for image synthesis. *Seminal Graphics Papers: Pushing the Boundaries, Volume 2*, 1993. [1](#)
- [10] Zilong Chen, Feng Wang, and Huaping Liu. Text-to-3d using gaussian splatting. *2024 IEEE/CVF Conference on Computer Vision and Pattern Recognition (CVPR)*, pages 21401–21412, 2023. [3](#)
- [11] Kai Cheng, Xiaoxiao Long, Kaizhi Yang, Yao Yao, Wei Yin, Yuexin Ma, Wenping Wang, and Xuejin Chen. Gaussianpro: 3d gaussian splatting with progressive propagation. *ArXiv*, abs/2402.14650, 2024. [3](#)
- [12] Xiaobiao Du, Yida Wang, and Xin Yu. Mvgs: Multi-view-regulated gaussian splatting for novel view synthesis, 2024. [1](#)
- [13] Guangchi Fang and Bing Wang. Mini-splatting: Representing scenes with a constrained number of gaussians. In *ECCV*, 2024. [1](#), [3](#), [5](#), [6](#), [7](#), [2](#)
- [14] Michael Goesele, Noah Snavely, Brian Curless, Hugues Hoppe, and Steven M. Seitz. Multi-view stereo for community photo collections. *2007 IEEE 11th International Conference on Computer Vision*, pages 1–8, 2007. [1](#)
- [15] Antoine Guédon and Vincent Lepetit. Sugar: Surface-aligned gaussian splatting for efficient 3d mesh reconstruction and high-quality mesh rendering. *2024 IEEE/CVF Conference on Computer Vision and Pattern Recognition (CVPR)*, pages 5354–5363, 2023. [3](#)
- [16] Zhiyang Guo, Wen gang Zhou, Li Li, Min Wang, and Houqiang Li. Motion-aware 3d gaussian splatting for efficient dynamic scene reconstruction. *ArXiv*, abs/2403.11447, 2024. [3](#)
- [17] Kaiming He, X. Zhang, Shaoqing Ren, and Jian Sun. Spatial pyramid pooling in deep convolutional networks for visual recognition. *IEEE Transactions on Pattern Analysis and Machine Intelligence*, 37:1904–1916, 2014. [3](#)
- [18] Peter Hedman, Julien Philip, True Price, Jan-Michael Frahm, George Drettakis, and Gabriel J. Brostow. Deep blending for free-viewpoint image-based rendering. *ACM Transactions on Graphics (TOG)*, 37:1 – 15, 2018. [2](#), [5](#), [6](#), [8](#), [1](#)
- [19] Peter Hedman, Pratul P. Srinivasan, Ben Mildenhall, Jonathan T. Barron, and Paul E. Debevec. Baking neural radiance fields for real-time view synthesis. *2021 IEEE/CVF International Conference on Computer Vision (ICCV)*, pages 5855–5864, 2021. [3](#)
- [20] Tao Hu, Shu Liu, Yilun Chen, Tiancheng Shen, and Jiaya Jia. Efficientnerf efficient neural radiance fields. In *Proceedings of the IEEE/CVF Conference on Computer Vision and Pattern Recognition (CVPR)*, pages 12902–12911, 2022. [3](#)
- [21] Binbin Huang, Zehao Yu, Anpei Chen, Andreas Geiger, and Shenghua Gao. 2d gaussian splatting for geometrically accurate radiance fields. In *SIGGRAPH 2024 Conference Papers*. Association for Computing Machinery, 2024. [3](#)
- [22] Ajay Jain, Matthew Tancik, and P. Abbeel. Putting nerf on a diet: Semantically consistent few-shot view synthesis. *2021 IEEE/CVF International Conference on Computer Vision (ICCV)*, pages 5865–5874, 2021. [3](#)
- [23] Tero Karras, Timo Aila, Samuli Laine, and Jaakko Lehtinen. Progressive growing of gans for improved quality, stability, and variation. *ArXiv*, abs/1710.10196, 2017. [3](#)
- [24] Bernhard Kerbl, Georgios Kopanas, Thomas Leimkuehler, and George Drettakis. 3d gaussian splatting for real-time radiance field rendering. *ACM Transactions on Graphics (TOG)*, 42:1 – 14, 2023. [1](#), [3](#), [4](#), [5](#), [6](#), [7](#), [2](#)
- [25] Arno Knapitsch, Jaesik Park, Qian-Yi Zhou, and Vladlen Koltun. Tanks and temples. *ACM Transactions on Graphics (TOG)*, 36:1 – 13, 2017. [2](#), [5](#), [6](#), [8](#), [1](#)
- [26] Agelos Kratimenos, Jiahui Lei, and Kostas Daniilidis. Dynmf: Neural motion factorization for real-time dynamic view synthesis with 3d gaussian splatting. *ArXiv*, abs/2312.00112, 2023. [3](#)
- [27] Minseop Kwak, Jiuhn Song, and Seung Wook Kim. Geconerf: Few-shot neural radiance fields via geometric consistency. *ArXiv*, abs/2301.10941, 2023. [3](#)
- [28] Chen-Hsuan Lin, Wei-Chiu Ma, Antonio Torralba, and Simon Lucey. Barf: Bundle-adjusting neural radiance fields. *2021 IEEE/CVF International Conference on Computer Vision (ICCV)*, pages 5721–5731, 2021. [3](#)

- [29] Tao Lu, Mulin Yu, Linning Xu, Yuanbo Xiangli, Limin Wang, Dahua Lin, and Bo Dai. Scaffold-gs: Structured 3d gaussians for view-adaptive rendering. *2024 IEEE/CVF Conference on Computer Vision and Pattern Recognition (CVPR)*, pages 20654–20664, 2023. 3, 5, 6, 2
- [30] Hidenobu Matsuki, Riku Murai, Paul H.J. Kelly, and Andrew J. Davison. Gaussian splatting slam. *2024 IEEE/CVF Conference on Computer Vision and Pattern Recognition (CVPR)*, pages 18039–18048, 2023. 3
- [31] Ben Mildenhall, Pratul P. Srinivasan, Matthew Tancik, Jonathan T. Barron, Ravi Ramamoorthi, and Ren Ng. Nerf: Representing scenes as neural radiance fields for view synthesis. In *ECCV*, 2020. 1, 3
- [32] Thomas Müller, Alex Evans, Christoph Schied, and Alexander Keller. Instant neural graphics primitives with a multiresolution hash encoding. *ACM Transactions on Graphics (TOG)*, 41:1 – 15, 2022. 1, 6, 2
- [33] Christian Reiser, Songyou Peng, Yiyi Liao, and Andreas Geiger. Kilonerf: Speeding up neural radiance fields with thousands of tiny mlps. *2021 IEEE/CVF International Conference on Computer Vision (ICCV)*, pages 14315–14325, 2021. 3
- [34] Christian Reiser, Richard Szeliski, Dor Verbin, Pratul P. Srinivasan, Ben Mildenhall, Andreas Geiger, Jonathan T. Barron, and Peter Hedman. Merf: Memory-efficient radiance fields for real-time view synthesis in unbounded scenes. *ACM Transactions on Graphics (TOG)*, 42:1 – 12, 2023. 3
- [35] Kerui Ren, Lihan Jiang, Tao Lu, Mulin Yu, Linning Xu, Zhangkai Ni, and Bo Dai. Octree-gs: Towards consistent real-time rendering with lod-structured 3d gaussians. *ArXiv*, abs/2403.17898, 2024. 3, 5, 6, 2
- [36] Andrei A. Rusu, Neil C. Rabinowitz, Guillaume Desjardins, Hubert Soyer, James Kirkpatrick, Koray Kavukcuoglu, Razvan Pascanu, and Raia Hadsell. Progressive neural networks. *ArXiv*, abs/1606.04671, 2016. 3
- [37] Jiaxiang Tang, Jiawei Ren, Hang Zhou, Ziwei Liu, and Gang Zeng. Dreamgaussian: Generative gaussian splatting for efficient 3d content creation. *ArXiv*, abs/2309.16653, 2023. 3
- [38] Zhou Wang, Alan Conrad Bovik, Hamid R. Sheikh, and Eero P. Simoncelli. Image quality assessment: from error visibility to structural similarity. *IEEE Transactions on Image Processing*, 13:600–612, 2004. 5
- [39] Guanjun Wu, Taoran Yi, Jiemin Fang, Lingxi Xie, Xiaopeng Zhang, Wei Wei, Wenyu Liu, Qi Tian, and Xinggang Wang. 4d gaussian splatting for real-time dynamic scene rendering. *2024 IEEE/CVF Conference on Computer Vision and Pattern Recognition (CVPR)*, pages 20310–20320, 2023. 3
- [40] Yuanbo Xiangli, Linning Xu, Xingang Pan, Nanxuan Zhao, Anyi Rao, Christian Theobalt, Bo Dai, and Dahua Lin. Bungeenerf: Progressive neural radiance field for extreme multi-scale scene rendering. In *European Conference on Computer Vision*, 2021. 3
- [41] Chi Yan, Delin Qu, Dong Wang, Dan Xu, Zhigang Wang, Bin Zhao, and Xuelong Li. Gs-slam: Dense visual slam with 3d gaussian splatting. *2024 IEEE/CVF Conference on Computer Vision and Pattern Recognition (CVPR)*, pages 19595–19604, 2023. 3
- [42] Zeyu Yang, Hongye Yang, Zijie Pan, Xiatian Zhu, and Li Zhang. Real-time photorealistic dynamic scene representation and rendering with 4d gaussian splatting. *ArXiv*, abs/2310.10642, 2023. 3
- [43] Zongxin Ye, Wenyu Li, Sidun Liu, Peng Qiao, and Yong Dou. Absgs: Recovering fine details in 3d gaussian splatting. *Proceedings of the 32nd ACM International Conference on Multimedia*, 2024. 1, 3, 5, 6, 7, 2
- [44] Taoran Yi, Jiemin Fang, Guanjun Wu, Lingxi Xie, Xiaopeng Zhang, Wenyu Liu, Qi Tian, and Xinggang Wang. Gaussian-dreamer: Fast generation from text to 3d gaussian splatting with point cloud priors. *ArXiv*, abs/2310.08529, 2023. 3
- [45] Alex Yu, Sara Fridovich-Keil, Matthew Tancik, Qinhong Chen, Benjamin Recht, and Angjoo Kanazawa. Plenoxels: Radiance fields without neural networks. *2022 IEEE/CVF Conference on Computer Vision and Pattern Recognition (CVPR)*, pages 5491–5500, 2021. 6, 2
- [46] Zehao Yu, Anpei Chen, Binbin Huang, Torsten Sattler, and Andreas Geiger. Mip-splatting: Alias-free 3d gaussian splatting. *2024 IEEE/CVF Conference on Computer Vision and Pattern Recognition (CVPR)*, pages 19447–19456, 2023. 3
- [47] Jingbo Zhang, Xiaoyu Li, Ziyu Wan, Can Wang, and Jing Liao. Fdnerf: Few-shot dynamic neural radiance fields for face reconstruction and expression editing. *SIGGRAPH Asia 2022 Conference Papers*, 2022. 3
- [48] Jiahui Zhang, Fangneng Zhan, Muyu Xu, Shijian Lu, and Eric P. Xing. Fregs: 3d gaussian splatting with progressive frequency regularization. *ArXiv*, abs/2403.06908, 2024. 1, 3, 5, 6, 2
- [49] Richard Zhang, Phillip Isola, Alexei A. Efros, Eli Shechtman, and Oliver Wang. The unreasonable effectiveness of deep features as a perceptual metric. *2018 IEEE/CVF Conference on Computer Vision and Pattern Recognition*, pages 586–595, 2018. 5
- [50] Zheng Zhang, Wenbo Hu, Yixing Lao, Tong He, and Hengshuang Zhao. Pixel-gs: Density control with pixel-aware gradient for 3d gaussian splatting. In *ECCV*, 2024. 1, 3, 6, 7, 2
- [51] Junyu Zhu, Hao Zhu, Qi Zhang, Fangfang Zhu, Zhan Ma, and Xun Cao. Pyramid nerf: Frequency guided fast radiance field optimization. *International Journal of Computer Vision*, 131:2649–2664, 2023. 3
- [52] Zi-Xin Zou, Zhipeng Yu, Yuanchen Guo, Yangguang Li, Ding Liang, Yan-Pei Cao, and Song-Hai Zhang. Triplane meets gaussian splatting: Fast and generalizable single-view 3d reconstruction with transformers. *2024 IEEE/CVF Conference on Computer Vision and Pattern Recognition (CVPR)*, pages 10324–10335, 2023. 3

ResGS: Residual Densification of 3D Gaussian for Efficient Detail Recovery

Supplementary Material

6. Additional Experiment Results

In this section, we provide additional experimental results of our work.

6.1. Variance of PSNR on Deep Blending Dataset

A notable variance in the PSNR metrics of our method is observed on the Deep Blending [18] dataset. We tested our method on the Deep Blending dataset 10 times and reported the average performance and population standard deviation. The results are shown in Table 5. The table demonstrates that the PSNR scores on the Deep Blending dataset exhibit a notable variance. The underlying reason, as discussed in our limitations, is that our method does not address issues related to occlusion and overfitting, making the Deep Blending dataset particularly challenging for our approach. This highlights opportunities for future optimization and improvement. Furthermore, we report the average performance and population standard deviation over 10 runs for the other two datasets, Mip-NeRF360 [1] and Tanks&Temples [25], as presented in Table 6 and Table 7, respectively. The PSNR metrics for these two datasets do not show a notable variance, showcasing the robustness of our method in most scenarios.

Table 5. Average and standard deviation results of three metrics on the Deep Blending dataset.

Dataset		Deep Blending					
Method	Metrics	PSNR \uparrow		SSIM \uparrow		LPIPS \downarrow	
		Avg	Stdev	Avg	Stdev	Avg	Stdev
Ours-Small (AbsGS)		29.71	0.211	0.903	0.002	0.235	0.002
Ours (3D-GS)		29.64	0.205	0.900	0.003	0.233	0.002
Ours (AbsGS)		29.68	0.173	0.900	0.002	0.228	0.002

Table 6. Average and standard deviation results of three metrics on the Mip-NeRF360 dataset.

Dataset		Mip-NeRF360					
Method	Metrics	PSNR \uparrow		SSIM \uparrow		LPIPS \downarrow	
		Avg	Stdev	Avg	Stdev	Avg	Stdev
Ours-Small (AbsGS)		27.93	0.010	0.830	0.001	0.191	0.001
Ours (3D-GS)		27.99	0.011	0.831	0.001	0.187	0.001
Ours (AbsGS)		27.99	0.011	0.833	0.001	0.174	0.001

Table 7. Average and standard deviation results of three metrics on the Tank&Temples dataset.

Dataset		Tank&Temples					
Method	Metrics	PSNR \uparrow		SSIM \uparrow		LPIPS \downarrow	
		Avg	Stdev	Avg	Stdev	Avg	Stdev
Ours-Small (AbsGS)		24.21	0.081	0.862	0.001	0.151	0.001
Ours (3D-GS)		24.26	0.058	0.864	0.001	0.141	0.001
Ours (AbsGS)		24.27	0.063	0.866	0.001	0.133	0.001

6.2. Further Analysis of Residual Split on 3D-GS

In our paper, we tested the compatibility of our residual split across multiple pipelines without modifying any hyper-parameters. Here, we present the results of applying residual split to 3D-GS [24] while adjusting the densification threshold τ to maintain the same storage size as 3D-GS, further demonstrating the capability of our method to enhance rendering quality. The results are shown in Table 8, showing that our method yields a further performance increase.

6.3. Periodic Opacity Reduction

3D-GS [24] often encounters redundancy issues, which we categorize into two main causes: the first is the use of an excessive number of small-scale Gaussians to represent coarse areas, and the second is the overlap between Gaussians, resulting in redundant Gaussians that contribute minimally to the rendered image. Our residual split can solve the first issue but does not address the second. To tackle the second issue, as mentioned in our experiment settings, we implemented the periodic opacity reduction technique in [5, 43]. Specifically, the opacity of Gaussians is periodically reduced, causing the opacity of those that contribute little to the rendered image to diminish to a negligible value, allowing them to be effectively pruned. Additionally, we extended this operation to occur after the densification stage, discovering that it further reduces redundancy without compromising fidelity. Here, we present the experimental results of our method without extending the periodic opacity reduction operation, as shown in Table 9. From the table, we can observe that extending the periodic opacity reduction operation effectively reduces redundancy without compromising the fidelity of the rendered images. Furthermore, when the operation is not extended and the gradient threshold is adjusted to maintain storage approximately equal to our full model, the rendering quality shows only a slight decrease in LPIPS metrics. This indicates that while extending the operation can enhance the performance of our method, its overall impact on the performance improvement is relatively minor.

Table 8. Results of residual split upon 3D-GS with varied gradient threshold.

Dataset		Mip-NeRF360				Tanks&Temples				Deep Blending			
Method	Metrics	PSNR ↑	SSIM ↑	LPIPS ↓	Mem	PSNR ↑	SSIM ↑	LPIPS ↓	Mem	PSNR ↑	SSIM ↑	LPIPS ↓	Mem
3D-GS		27.21	0.815	0.214	734MB	23.14	0.841	0.183	411MB	29.41	0.903	0.243	676MB
3D-GS + residual split		27.48	0.815	0.213	722MB	23.85	0.846	0.174	374MB	29.83	0.901	0.238	640MB

Table 9. Results of our method without extended periodic opacity reduction. Here, **No EPOR** refers to our method trained without applying the extended periodic opacity reduction. **No EPOR + CT** refers to the model without the extended periodic opacity reduction but with an adjusted gradient threshold to ensure that the final storage size is approximately the same as our full model with extended periodic opacity reduction.

Dataset		Mip-NeRF360				Tanks&Temples				Deep Blending			
Method	Metrics	PSNR ↑	SSIM ↑	LPIPS ↓	Mem	PSNR ↑	SSIM ↑	LPIPS ↓	Mem	PSNR ↑	SSIM ↑	LPIPS ↓	Mem
Ours (No EPOR)		28.02	0.833	0.173	973MB	24.32	0.867	0.130	591MB	29.86	0.902	0.227	911MB
Ours (No EPOR + CT)		28.00	0.833	0.181	608MB	24.35	0.866	0.139	380MB	29.96	0.904	0.230	564MB
Ours (full)		28.00	0.833	0.174	698MB	24.38	0.867	0.132	351MB	29.91	0.902	0.227	586MB

6.4. Image Resolution of Mip-NeRF360 Dataset

In our paper, we mentioned that the image resolution on the Mip-NeRF360 [1] dataset varies across different works. 3D-GS [24] uses the provided “images_4”, the official downsampled 4 times images from the dataset, for outdoor scenes and “images_2” for indoor scenes. Most works [13, 43, 48] follow the 3D-GS setting, but Scaffold-GS [29], Octree-GS [35], Pixel-GS [50] uses different settings. Specifically, Scaffold-GS and Octree-GS downscale original images to 1.6K resolution, while Pixel-GS downscales original images by a factor of 4 for outdoor scenes and 2 for indoor scenes during the training process, instead of using the provided downsampled images. This discrepancy results in differences in experimental settings. To further demonstrate the performance of our method, we provide its results under the two different settings, as shown in Table 10 and 11. The tables show that our method prevails even under these alternate settings.

Table 10. Results on the Mip-NeRF360 dataset with same setting as Scaffold-GS and Octree-GS.

Dataset		Mip-NeRF360		
Method	Metrics	PSNR ↑	SSIM ↑	LPIPS ↓
Scaffold-GS		27.71	0.813	0.221
Octree-GS		27.73	0.815	0.217
Ours-Small (AbsGS)		28.04	0.831	0.191
Ours (3D-GS)		28.10	0.832	0.187
Ours (AbsGS)		28.14	0.834	0.174

Table 11. Results on the Mip-NeRF360 dataset with same setting as Pixel-GS.

Dataset		Mip-NeRF360		
Method	Metrics	PSNR ↑	SSIM ↑	LPIPS ↓
Pixel-GS		27.88	0.834	0.176
Ours-Small (AbsGS)		28.21	0.841	0.176
Ours (3D-GS)		28.28	0.843	0.172
Ours (AbsGS)		28.30	0.845	0.160

6.5. Per Scene Results

We present the per-scene results of the used metrics in Table 12-17. For works that did not report per-scene results, we obtained and reported them using their released code. The works selected for comparison are mainly the same as in the paper: 3D-GS [24], Scaffold-GS [29], Octree-GS [35], AbsGS [43], Pixel-GS [50], Mini-Splatting-D [13], Plenoxels [45], Instant-NGP [32] and Mip-NeRF360 [1]. Note that we did not show the results of FreGS [48] since they did not report their per-scene results or release their code. Works retrained on the Mip-NeRF360 [1] are marked with a *.

Table 12. Per-scene PSNR metrics of Mip-NeRF360 dataset.

Method	Scenes	bicycle	flowers	garden	stump	treehill	room	counter	kitchen	bonsai
Plenoxels		21.91	20.10	23.49	20.66	22.25	27.59	23.62	23.42	24.67
Instant-NGP		22.17	20.65	25.07	23.47	22.37	29.69	26.69	29.48	30.69
Mip-NeRF360		24.31	21.65	26.88	26.18	22.93	31.47	29.45	31.99	33.40
Scaffold-GS*		25.07	21.36	27.35	26.64	22.93	32.04	29.50	31.63	32.71
Octree-GS*		25.05	21.33	27.58	26.41	22.81	32.09	29.48	30.89	31.71
3D-GS		25.25	21.52	27.41	26.55	22.49	30.63	28.70	30.32	31.98
AbsGS		25.29	21.35	27.48	26.71	21.99	31.61	29.03	31.62	32.32
Pixel-GS*		25.21	21.49	27.42	26.84	22.09	31.45	29.05	31.65	32.53
Mini-Splatting-D		25.55	21.50	27.67	27.11	22.13	31.41	28.72	31.75	31.72
Ours-Small (AbsGS)		25.62	21.80	27.72	27.27	22.90	32.41	29.32	31.95	32.48
Ours (3D-GS)		25.55	22.07	27.71	27.12	22.82	32.48	29.41	32.09	32.74
Ours (AbsGS)		25.62	21.78	27.82	27.19	22.57	32.51	29.50	32.26	32.78

Table 13. Per-scene SSIM metrics of Mip-NeRF360 dataset.

Method	Scenes	bicycle	flowers	garden	stump	treehill	room	counter	kitchen	bonsai
Plenoxels		0.496	0.431	0.6063	0.523	0.509	0.8417	0.759	0.648	0.814
Instant-NGP		0.512	0.486	0.701	0.594	0.542	0.871	0.817	0.858	0.906
Mip-NeRF360		0.685	0.584	0.809	0.745	0.631	0.910	0.892	0.917	0.938
Scaffold-GS*		0.755	0.590	0.858	0.765	0.639	0.923	0.910	0.926	0.943
Octree-GS*		0.759	0.597	0.864	0.763	0.643	0.924	0.907	0.916	0.930
3D-GS		0.771	0.605	0.868	0.775	0.638	0.914	0.905	0.922	0.938
AbsGS		0.783	0.623	0.871	0.780	0.617	0.925	0.911	0.929	0.945
Pixel-GS*		0.775	0.633	0.867	0.784	0.630	0.920	0.911	0.929	0.944
Mini-Splatting-D		0.798	0.642	0.878	0.804	0.640	0.928	0.913	0.934	0.946
Ours-Small (AbsGS)		0.792	0.634	0.872	0.802	0.652	0.929	0.914	0.932	0.945
Ours (3D-GS)		0.790	0.639	0.874	0.800	0.650	0.929	0.916	0.934	0.947
Ours (AbsGS)		0.797	0.647	0.876	0.804	0.645	0.931	0.918	0.934	0.948

Table 14. Per-scene LPIPS metrics of Mip-NeRF360 dataset.

Method	Scenes	bicycle	flowers	garden	stump	treehill	room	counter	kitchen	bonsai
Plenoxels		0.506	0.521	0.3864	0.503	0.540	0.4186	0.441	0.447	0.398
Instant-NGP		0.446	0.441	0.257	0.421	0.450	0.261	0.306	0.195	0.205
Mip-NeRF360		0.301	0.344	0.170	0.261	0.339	0.211	0.204	0.127	0.176
Scaffold-GS*		0.233	0.352	0.120	0.236	0.331	0.216	0.203	0.130	0.207
Octree-GS*		0.225	0.340	0.108	0.233	0.310	0.203	0.202	0.141	0.219
3D-GS		0.205	0.336	0.103	0.210	0.317	0.220	0.204	0.129	0.205
AbsGS		0.171	0.270	0.100	0.195	0.278	0.200	0.189	0.121	0.190
Pixel-GS*		0.182	0.263	0.100	0.186	0.280	0.213	0.185	0.120	0.193
Mini-Splatting-D		0.158	0.255	0.090	0.169	0.262	0.190	0.172	0.114	0.175
Ours-Small (AbsGS)		0.175	0.290	0.099	0.188	0.279	0.196	0.184	0.117	0.189
Ours (3D-GS)		0.168	0.295	0.092	0.179	0.280	0.192	0.177	0.114	0.185
Ours (AbsGS)		0.156	0.251	0.089	0.170	0.250	0.187	0.172	0.112	0.179

Table 15. Per-scene PSNR metrics of Tank&Temples and Deep Blending dataset.

Method Scenes	Truck	Train	Dr Johnson	Playroom
Plenoxels	23.22	18.93	23.14	22.98
Instant-NGP	23.38	20.46	28.26	21.67
Mip-NeRF360	24.91	19.52	29.14	29.66
Scaffold-GS	25.77	22.15	29.80	30.62
Octree-GS	26.27	22.77	29.87	30.95
3D-GS	25.19	21.10	28.77	30.04
AbsGS	25.74	21.72	29.20	30.14
Pixel-GS	25.49	22.13	28.02	29.79
Mini-Splatting-D	25.43	21.04	29.32	30.43
Ours-Small (AbsGS)	26.07	22.40	29.64	30.38
Ours (3D-GS)	26.08	22.65	29.54	30.32
Ours (AbsGS)	26.14	22.61	29.51	30.32

Table 16. Per-scene SSIM metrics of Tank&Temples and Deep Blending dataset.

Method Scenes	Truck	Train	Dr Johnson	Playroom
Plenoxels	0.774	0.663	0.787	0.802
Instant-NGP	0.800	0.689	0.854	0.779
Mip-NeRF360	0.857	0.660	0.901	0.900
Scaffold-GS	0.883	0.822	0.907	0.904
Octree-GS	0.896	0.835	0.912	0.914
3D-GS	0.879	0.802	0.899	0.906
AbsGS	0.888	0.818	0.898	0.907
Pixel-GS	0.883	0.823	0.885	0.899
Mini-Splatting-D	0.890	0.817	0.905	0.908
Ours-Small (AbsGS)	0.889	0.834	0.905	0.907
Ours (3D-GS)	0.890	0.840	0.901	0.905
Ours (AbsGS)	0.893	0.841	0.900	0.905

Table 17. Per-scene LPIPS metrics of Tank&Temples and Deep Blending dataset.

Method Scenes	Truck	Train	Dr Johnson	Playroom
Plenoxels	0.335	0.422	0.521	0.499
Instant-NGP	0.249	0.360	0.352	0.428
Mip-NeRF360	0.159	0.354	0.237	0.252
Scaffold-GS	0.147	0.206	0.250	0.258
Octree-GS	0.118	0.198	0.231	0.244
3D-GS	0.148	0.218	0.244	0.241
AbsGS	0.132	0.193	0.241	0.233
Pixel-GS	0.122	0.180	0.258	0.243
Mini-Splatting-D	0.100	0.181	0.218	0.204
Ours-Small (AbsGS)	0.124	0.177	0.233	0.235
Ours (3D-GS)	0.118	0.164	0.232	0.231
Ours (AbsGS)	0.106	0.159	0.231	0.223